




Prebifurcation enhancement of imbibition-drainage hysteresis cyclesIdo Lavi,^{1,2} Lauren Rose,³ Ramon Planet,¹ Jaume Casademunt ¹,
Stéphane Santucci ³ and Jordi Ortín ¹¹*Departament de Física de la Matèria Condensada, Universitat de Barcelona, Martí i Franquès 1, 08028 Barcelona, Spain and UBICS (University of Barcelona Institute of Complex Systems)*²*Center for Computational Biology, Flatiron Institute, 162 5th Ave, New York, New York 10010, USA*³*Univ Lyon, ENS de Lyon, CNRS, Laboratoire de Physique, F-69342 Lyon, France*

(Received 23 April 2023; accepted 27 November 2023; published 20 December 2023)

The efficient transport of fluids through disordered media requires a thorough understanding of how the driving rate affects two-phase interface propagation. Despite our understanding of front dynamics in homogeneous environments, as well as how medium heterogeneities shape fluid interfaces at rest, little is known about the effects of localized topographical variations on large-scale interface dynamics. To gain physical insights into this problem, we study here oil-air displacements through an “imperfect” Hele-Shaw cell. Combining experiments, numerical simulations, and theory, we show that the flow rate dramatically alters the interface response to a porous constriction as one approaches the Saffman-Taylor instability, strictly under stable conditions. This gives rise to asymmetric imbibition–drainage hysteresis cycles that feature divergent extensions and nonlocal effects, all of which are aptly captured and explained by a minimal free boundary model.

DOI: [10.1103/PhysRevFluids.8.124002](https://doi.org/10.1103/PhysRevFluids.8.124002)**I. INTRODUCTION**

Multiphase flows through porous media play an essential role in a variety of natural and engineered processes, including sap circulation in plants, CO₂ storage, oil recovery, filtering, and printing [1,2]. Despite extensive research, predicting how local medium heterogeneities of different types alter the large-scale displacements of fluid-fluid interfaces remains a major challenge [3–5]. Recent studies focused on the effects of changing the fluid wetting properties [6–10], while the impact of the displacement rate and its interplay with sharp heterogeneities of the solid matrix has received less attention [11–15]. Back in 1986, de Gennes suggested that a narrow channel with localized chemical or topographical defects would be a relevant system for studying the complexities of multiphase flows in disordered media [16]. Such “imperfect” Hele-Shaw (HS) cells have since been used to address a variety of interesting problems, including viscous fingering alterations [17–19], fluid trapping [20,21], bubble and foam dynamics [22,23], capillary rise [24,25], kinetic roughening [26,27], avalanches of fluid fronts [28–30], and the emergence of pressure-saturation hysteresis cycles [31,32]. Such hysteresis loops present a problem of high relevance in hydrology and engineering. Until recently, this behavior was addressed from a purely phenomenological perspective.

Here, we use an “imperfect” HS cell to clarify the time-dependent response of an advancing fluid interface to an elongated constriction. Examining a simplified model system containing only one topographic defect, we gain a clear and measurable understanding of the local and nonlocal interface response in various stages: preinvasion, contact phase, and depinning. Correctly delineating these elementary processes can help understand the emergence of hysteretic flows in more complex disordered media. By varying the flow rate in this study, we extend upon previous research that was

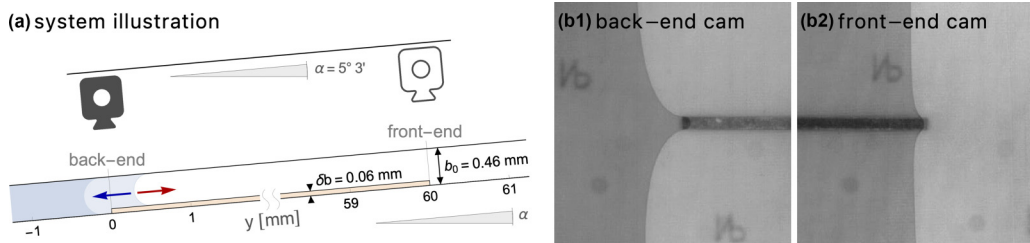


FIG. 1. Setup and sample images. (a) Schematic y - z side view of our tilted HS cell near the back-end and front-end of the mesa (light orange). Red (blue) arrow indicates the direction of oil propagation in imbibition (drainage). (b1,b2) Sample images from two separate experiments, captured from above the back-end or front-end of the mesa.

restricted to quasistatic driving [31,32]. We show experimentally that increasing flow rates for oil-air displacements suppress the interface deformation in imbibition and amplify it in drainage, still under stable Saffman-Taylor (S-T) conditions. We interpret this bias as a prebifurcation enhancement: the interface becomes more susceptible to the defect as one approaches the S-T instability. We further show that finite flow rates in both directions trigger nonlocal effects associated with mass conservation. The mechanisms underlying these phenomena are clarified through our theoretical and numerical analysis of the gap-varying HS problem. The insights gained from this study are relevant to any pair of fluids that are displaced through similar heterogeneities.

II. METHODS

A. Experimental setup

We fabricated a rectangular chamber, of width $W = 190$ mm, made of two parallel glass plates separated by a small gap, $b_0 = 0.46 \pm 0.02$ mm. At the center of the bottom plate, we fixed a mesa-shaped constriction of thickness $\delta b = 0.060 \pm 0.003$ mm, width $w = 3.00 \pm 0.05$ mm, and length $l = 60.00 \pm 0.05$ mm (see Fig. 1). By tilting the cell y axis at an angle $\alpha = 5^\circ 3' \pm 2'$ with respect to the horizontal, we set the effective gravity to $-g_e \hat{y}$, where $g_e = g \sin \alpha$. At the cell inlet or outlet (positioned beneath $y = -100$ mm), we used a syringe pump to inject or withdraw a silicone oil (viscosity $\mu = 51.6 \pm 0.6$ cP, density $\rho = 972 \pm 4$ kg/m³, surface tension with air $\gamma = 21.0 \pm 1.3$ mN/m) at a constant rate, leading to a velocity $V_0 \hat{y}$ of the fluid (positive in imbibition, negative in drainage). Our top-view camera (resolution: 0.16 mm/px, frame rate: 100 fps) imaged the free oil-air interface as it traversed the constriction. Displacements were limited to linearly stable conditions, meaning $\text{Ca} + \text{Bo} > 0$, where $\text{Ca} = \Delta\mu V_0 / \gamma$ and $\text{Bo} = k_0 g_e \Delta\rho / \gamma$ are the capillary and Bond numbers. Here, $k_0 = b_0^2 / 12$ is the hydraulic permeability of the homogeneous cell. The oil-air differences in viscosity and density, $\Delta\mu$ and $\Delta\rho$, are well approximated by μ and ρ of the oil phase alone. Stable drainage displacements were thus possible in the range $-k_0 g_e \rho / \mu < V_0 < 0$.

B. Model equations and numerical solution

Assuming small modulations in the cell height $b(x, y)$, and neglecting pressure gradients in the air, the gap-averaged two-dimensional (2D) flow \mathbf{u} and pressure p of the oil solve the free-boundary problem

$$\mathbf{u} = \frac{k}{\mu} (-\nabla p - g_e \rho \hat{y}), \quad \nabla \cdot (b \mathbf{u}) = 0, \quad \text{in } \Omega(t), \quad (1)$$

$$p = \gamma \left(\frac{\pi}{4} \kappa - \frac{2}{b} \right), \quad V_n = \mathbf{u} \cdot \mathbf{n}, \quad \text{on } \Gamma_1(t), \quad (2)$$

where $\Omega(t)$ is the projected oil domain and $\Gamma_1(t)$ is the oil-air interface. The first equation is Darcy's law, with $k(x, y) = b(x, y)^2/12$ the varying cell permeability [33]. The second equation imposes volumetric incompressibility, and is equivalent to $\nabla \cdot \mathbf{u} = -\mathbf{u} \cdot \nabla b/b$. This means that sources or sinks in the effective 2D problem emerge where the fluid moves against a spacing gradient. In Eq. (2), we present first the Young-Laplace condition, with κ denoting the in-plane curvature. For simplicity, we assume that the oil perfectly wets the top and bottom surfaces, implying prewetting conditions for imbibition [34], and also neglect the thickness of the oil layers coating the cell plates, which depends nontrivially on the local Ca [35–37]. The last equation in (2) is the kinematic condition, with V_n the sharp interface velocity. We further impose no-flux conditions at the lateral cell walls: $u_x = 0$ at $x = \pm W/2$, and the driving speed at the cell inlet/outlet: $u_y = V_0$ at $y = -L$ (see detailed summary in Appendix A).

We developed a finite-element (FE) solver of the moving-boundary-value problem, implemented in FREEFEM++ [38]. Our scheme, detailed in Appendix B, features (i) a sharp-interface discretization with an implicit variational treatment of the curvature κ [39,40], and (ii) a dynamic adaptive mesh, determined by the mesa geometry and the evolving interface Γ_1 .

III. RESULTS

A. Displacements through a mesa constriction

Figure 2 shows the evolution of the oil-air interface during oil injection (imbibition, in red) and withdrawal (drainage, in blue). Experimental and computational results for both slow and fast driving velocities are presented for comparison. Over the mesa cross-section, the curvature of the oil-air meniscus increases abruptly [see Fig. 1(a)]. Since oil is wetting the surfaces, this local capillary jump pulls the interface forward. The tension force associated with the in-plane curvature, as well as the viscous and gravitational forces in the bulk, produce a centered bell-shaped protrusion that decays on the sides of the mesa. To facilitate trajectory comparisons, we define a deformation amplitude η that measures the distance from the tip of the protrusion, at $x = 0$, to a baseline, defined arbitrarily as the mean interface height at a lateral distance $d = 3w = 9$ mm (see Fig. 2). In Fig. 3, we plot η as a function of the displaced baseline.

In imbibition (red, advancing from left to right in Figs. 2 and 3), we understand the trajectory as follows. Before coming in contact with the mesa, the interface is under constant gap height and remains flat ($\eta = 0$). Upon first contact, the local capillary jump induces the protrusion. As this happens rapidly, mass conservation imposes that lateral segments of the interface may retract backwards in the frame of reference that moves with V_0 . This effect is captured experimentally and theoretically for low driving speeds [see dark red curve in Fig. 3(b)]. Ultimately, a new steady-state profile is reached as the oil continues to displace the air at a constant rate. Faster imbibition speeds produce flatter steady states (lighter red curves in Fig. 3). At the front-end of the mesa, the interface tip is effectively pinned because it is no longer pulled preferentially towards air [note the sharp corner of the red curve in Fig. 3(c)]. For low velocities, the interface is completely flattened by the time it clears the front-end [dark red curve in Fig. 3(d)]. However, at large finite speeds the viscous relaxation to the flat state can be slower than the displacement itself: the tip surpasses the constriction while the interface is still deformed [see light red curve in Fig. 3(d)].

In drainage (blue, advancing from right to left in Figs. 2 and 3), air is displacing the oil while the fingering instability is avoided. Before first contact with the mesa front-end, the interface remains flat if the driving speed is low [see dark blue curve in Fig. 3(d)]. For large speeds, the interface begins to deform already at this stage [light blue curve in Fig. 3(d)]. This nonlocal effect is triggered by volumetric incompressibility on the front-end, which acts as an effective 2D source when embedded in the drained oil phase. Once contact is made, the central tip of the interface is pinned, as in imbibition. For low velocities, the tip passes this edge when the interface reaches the new deformed steady state [note the sharp corner of the dark blue curve in Fig. 3(c)]. For large speeds, this happens while the deformation continues to grow [light blue curve in Fig. 3(c)]. In fact, the interface may

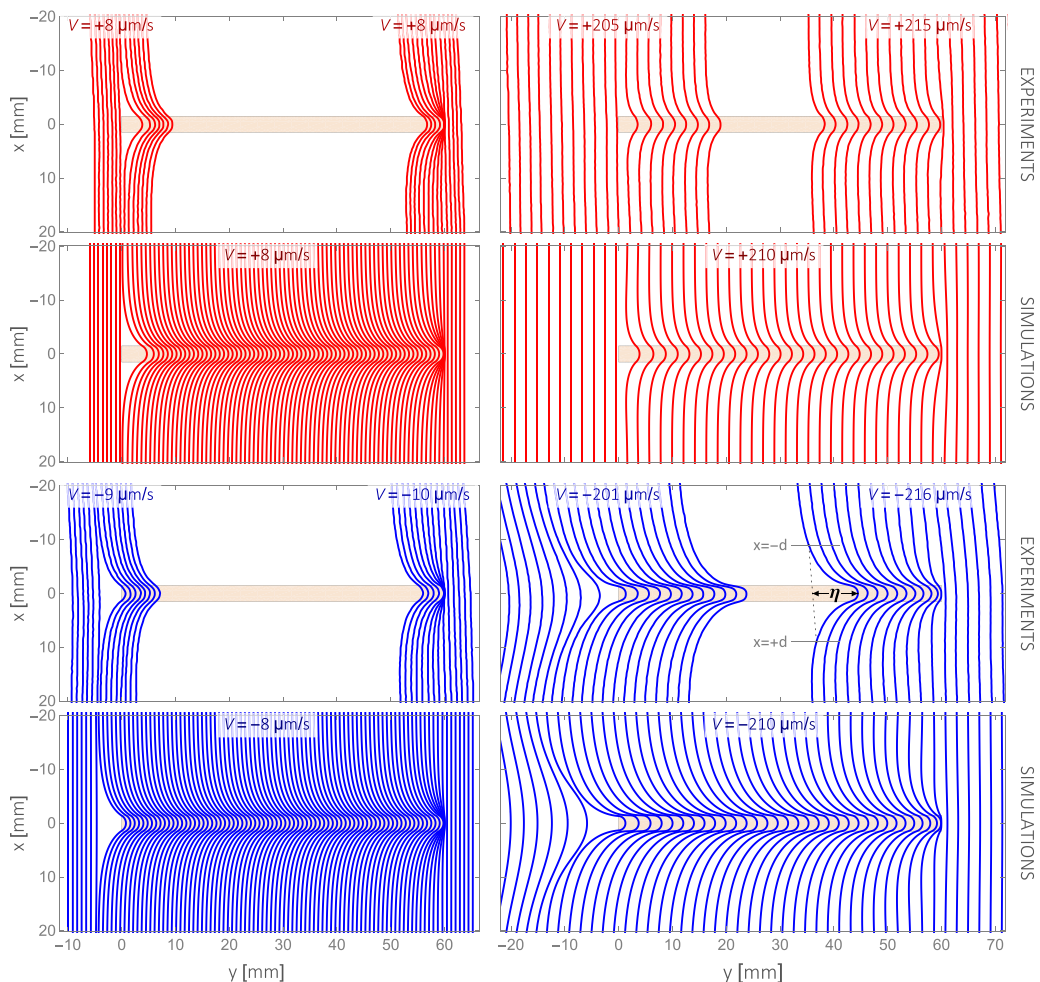


FIG. 2. Oil-air displacements through a mesa constriction at increasing flow rates. Top views of the experimental and computational interface evolution during imbibition (red, advancing from left to right) and drainage (blue, advancing from right to left). Interface profiles are presented in intervals of $\Delta t = 100$ s for low velocities (left panels) and $\Delta t = 10$ s for high velocities (right panels). We define the deformation measure η as shown in the bottom right experimental panel, with $d = 9$ mm.

not even reach steady state by the time it had fully cleared the length of the mesa (η does not level out). Moreover, in this case the deformation begins to decrease gradually before the tip reaches the back-end [see Fig. 3(a)]. This nonlocal effect is attributed to the back-end of the mesa acting as an effective 2D sink. The depinning dynamics also vary as a function of V_0 . Higher drainage speeds prolong the interface relaxation by increasing the viscous resistance, as explained by a linear stability analysis (see Appendix C). For low drainage speeds, as in imbibition, the rapid relaxation of the interface leads to retraction of lateral segments in the moving frame of reference [see dark blue curve in Fig. 3(b)].

Importantly, the depinning point in drainage is distinct from the point of first contact in imbibition. This is true also for quasistatic displacements owing to the bistability of hydrostatic states [31,41]. Our study shows that finite driving speeds accentuate the difference between the two displacement directions, thereby producing highly “asymmetric” hysteresis cycles.

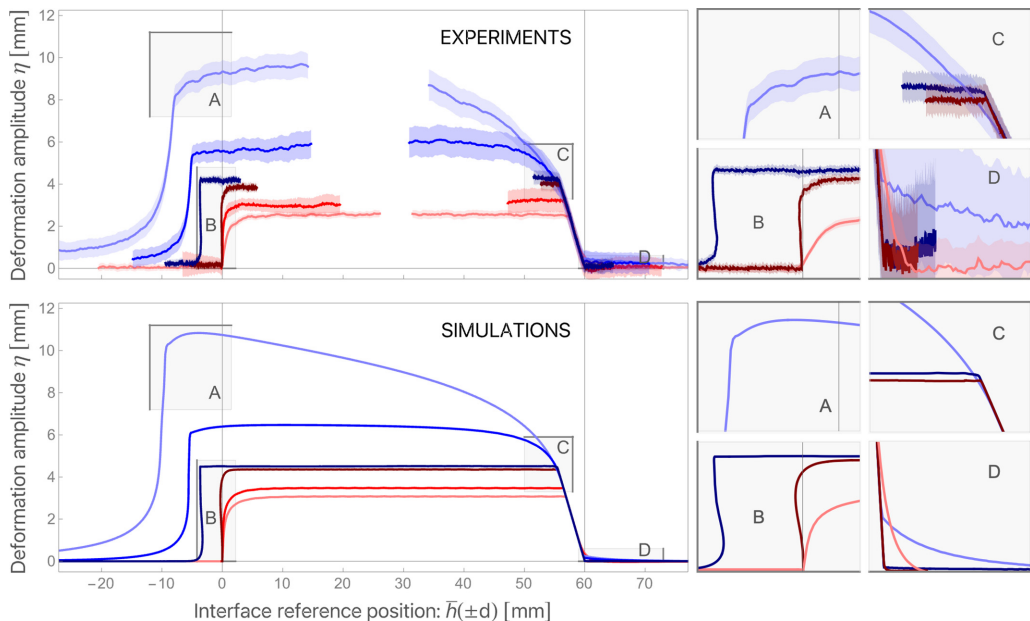


FIG. 3. Asymmetric imbibition-drainage hysteresis cycles. Top left: The deformation amplitude $\eta = h(0) - \bar{h}(\pm d)$ is plotted with confidence $|h(d) - h(-d)|$ against the interface reference position, $\bar{h}(\pm d) = (h(d) + h(-d))/2$, for drainage or imbibition experiments (blue or red curves). Lighter colors correspond to faster speeds. Increasing the displacement rate in drainage (imbibition) gives rise to stronger (weaker) deformations. Experimental drainage speeds are $V_0 = \{-216 \pm 14, -139 \pm 9, -10 \pm 1\} \mu\text{m/s}$ about the front-end of the mesa and $V_0 = \{-201 \pm 14, -126 \pm 10, -9 \pm 2\} \mu\text{m/s}$ about the back-end. Experimental imbibition speeds are $V_0 = \{8 \pm 2, 51 \pm 4, 205 \pm 14\} \mu\text{m/s}$ about the front-end of the mesa and $V_0 = \{8 \pm 1, 52 \pm 4, 215 \pm 14\} \mu\text{m/s}$ about the back-end. Bottom left: Same plots for FE simulations with drainage speeds $V_0 = \{-210, -130, -8\} \mu\text{m/s}$ (light to dark blue) and imbibition speeds $V_0 = \{8, 130, 210\} \mu\text{m/s}$ (dark to light red). Right boxes: Zooms highlighting different corners of the trajectories, excluding intermediate velocities for clarity.

B. Steady interface deformations

We gain further insight by deriving the steady profile of a moving oil front that traverses the elongated constriction. To this end, we assume that the oil is displaced uniformly, with $\mathbf{u} = V_0 \hat{y}$ in $\Omega(t)$, over an infinitely long mesa, $b = b_0 - \delta b \text{rect}(x/w)$ (no y dependence). It follows from Eqs. (1) and (2) that the interface profile in the moving frame of reference, $h(x) := y(x, t) - V_0 t$, solves the nonlinear ordinary-differential-equation (ODE)

$$-\left(\frac{\mu}{k(x)} V_0 + g_e \rho\right) h(x) = \gamma \left(\frac{\pi}{4} \kappa(x) - \frac{2}{b(x)} + \frac{2}{b_0} \right), \quad (3)$$

where $\kappa(x) = -h''(x)/[1 + h'(x)^2]^{3/2}$.

In the limits $\delta b/b_0 \ll 1$ and $|h'| \ll 1$, the steady front profile is approximated by

$$h(x) = \frac{8}{\pi} \left(\frac{\ell_c}{b_0} \right)^2 \delta b \begin{cases} 1 - e^{-w/2\ell_c} \cosh\left(\frac{x}{\ell_c}\right), & |x| \leq \frac{w}{2}, \\ \sinh\left(\frac{w}{2\ell_c}\right) e^{-|x|/\ell_c}, & |x| > \frac{w}{2}, \end{cases} \quad (4)$$

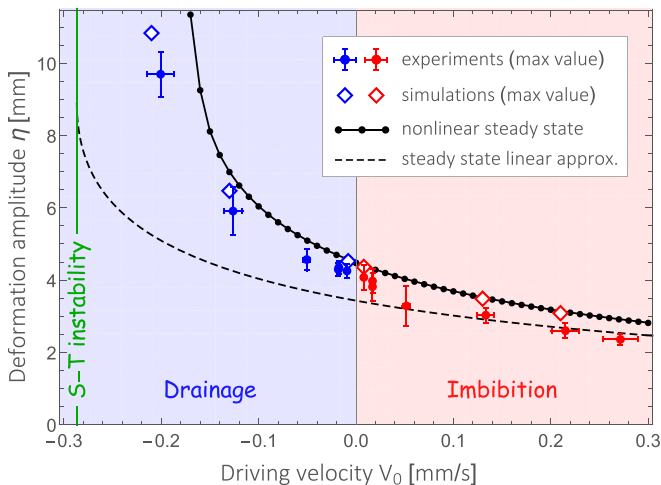


FIG. 4. Impact of flow rate on steady deformations. Measured and computed values of the deformation amplitude η as a function of the driving speed V_0 . Green line marks the threshold of the Saffman-Taylor instability, where $Ca = -Bo$.

where ℓ_c is the capillary length

$$\ell_c = \sqrt{\frac{k_0\pi/4}{Ca + Bo}},$$

as shown in Appendix D (and similarly in Ref. [32] for the quasistatic case). This linear approximation captures well the qualitative features of the measured profiles: the bell-shaped tip with exponentially decaying wings, the discontinuous second derivative on the lateral mesa edges ($x = \pm w/2$), and the negative dependence of the deformation on V_0 (see Fig. 7 in Appendix D). However, we find that the linear curvature assumption, $|h'| \ll 1$, does not hold well in our experimental regime (see Fig. 8 in Appendix D).

To solve the exact Eq. (3) computationally, one must specify two boundary conditions. One of these, $h(x=0)$, is unknown *a priori* and should be varied to satisfy $h \rightarrow 0$ as $x \rightarrow \pm\infty$. We resolved this problem through a dedicated “shooting method” explained in Appendix D. Compared with the linear approximation, the nonlinear solution points to stronger deformations, particularly in drainage, that are more in line with observations. We also used these results to verify our dynamic FE simulations (see Fig. 9 in Appendix D).

Figure 4 summarizes the experimental and theoretical dependence of the deformation amplitude η on the driving speed. Specifically, we show (i) the maximal deformation measured experimentally, (ii) the maximal deformation in our FE simulations [integration of Eqs. (1)–(2)], (iii) the nonlinear steady state [computational solution of Eq. (3)], and (iv) the steady-state linear approximation [Eq. (4)]. Without a single fitting parameter, we find remarkable quantitative agreement between the nonlinear theory and our experiments. In imbibition, the small deviation of experiments from the theory may be due to the presence of prewetting films. At high drainage speeds, the deviation of both experiments and FE simulations from the nonlinear steady-state prediction is expected: in this regime the interface completely cleared the length of the mesa before a steady state could be reached.

Oil withdrawal that is maintained close to the onset of the S-T instability may lead to extreme transient deformations. As shown in Fig. 5(a1), a necking phenomenon ensues beneath the back-end of the mesa while the tip of the interface still lingers on the constriction. The eventual detachment of the tip gives way to highly nonlinear depinning dynamics [Fig. 5(a2)]. Such observations are

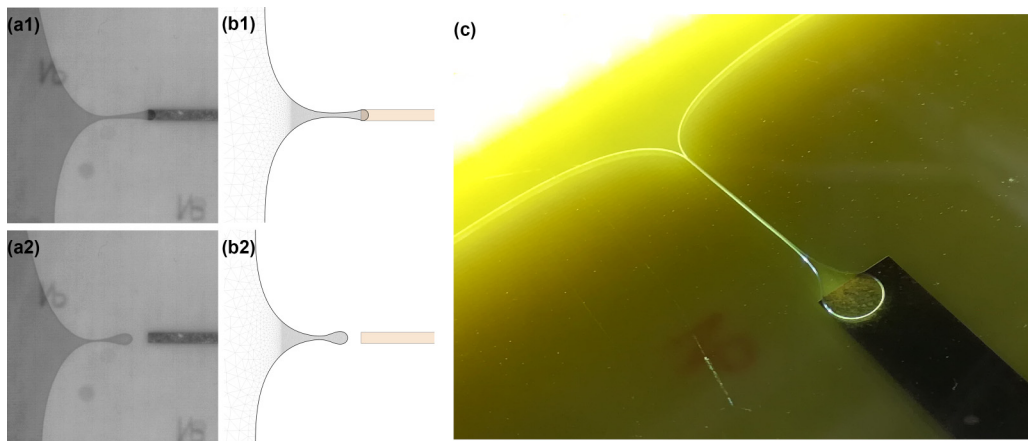


FIG. 5. Extreme front deformations and nonlinear depinning from the back-end. (a1,a2) Experimental images separated by 10 s, captured in the course of oil withdrawal with $V_0 = -255 \pm 17 \mu\text{m}$. (b1,b2) Mesh and interface of a moving computational domain separated by 10 s, taken from a drainage simulation with $V_0 = -260 \mu\text{m}$. (c) Thin filament produced by quasistatic oil withdrawal through a wider mesa ($w = 9 \text{ mm}$) with a lower inclination of the cell ($\alpha = 2^\circ 21'$), meaning lower Bo . This picture was captured manually from an oblique angle using a different type of illumination.

predicted by the model and can be effectively captured in our FE simulations, provided adequate resolution and frequent remeshing [Figs. 5(b1) and 5(b2)]. Notwithstanding, our current comparisons are mainly qualitative in nature due to the challenging sensitivity of this limit. In quasistatic experiments with different geometrical conditions (wider mesa, lower inclination) we observe the formation of a slender and straight thread of connected interface [Fig. 5(c)]. This scenario eventually results in a pinch-off event and the entrapment of a separated oil drop. It is acknowledged that our sharp-interface simulations are not well suited for addressing singularities of this type. Leastwise, as the neck width becomes comparable to the gap height b_0 , the assumptions that underlie the 2D equations are no longer valid.

IV. DISCUSSION AND CONCLUSION

Our findings showcase the prebifurcation enhancement of the interface response to a constriction in an idealized porous medium. All displacements were performed under stable S-T conditions, such that the interface would flatten out if the cell was homogeneous. However, in the presence of a weak topographic heterogeneity, the proximity to the fingering instability is shown to be highly impactful. For increasing drainage speeds, the deformation tends to diverge as the interface extends straight segments along the side edges of the mesa. This preinstability finger reflects a balance between the tendency to maximize the total wetted area (promoted by a decrease in the pressure gradient) and the tendency to minimize the interfacial perimeter (due to surface tension) for a given volume of fluid.

We further demonstrated a rich dynamic phenomenology that emerges in this simple one-defect setup. Time-dependent imbibition or drainage displacements are captured in great detail by a reduced 2D model that neglects the dynamic contact angle and wetting layer thickness. The local capillary perturbation is explicitly injected in the problem through the Young-Laplace condition in Eq. (2). Nonlocal effects mediated by the fluid bulk are evidently attributable to volume conservation via the incompressibility condition in Eq. (1). In general, the interface dynamics are also affected nonlocally by spatial variations in the permeability, $k = b^2/12$ [33]. This is captured by the equations but negligible in our system because $\delta b \ll b_0$.

A natural extension of this study is to consider many constrictions and/or expansions simultaneously to emulate a spatially extended disordered medium. The presence of multiple defects is known to give rise to cooperative phenomena in the form of large-scale avalanches. We expect such complex displacements to be even more sensitive to the driving rate, owing to the local and nonlocal effects described in this paper. The experimental and numerical tools presented here could be directly extended to a variety of fluid pairs and geometries to yield further physical insights and quantitative predictions.

ACKNOWLEDGMENTS

Financial support from MICINN (the Spanish Ministry of Science and Innovation) through Projects No. PID2019-106887GB-C32 (J.O.) and No. PID2019-108842GB-C21 (I.L. and J.C.) is gratefully acknowledged. J.C., I.L., J.O., and R.P. were supported by AGAUR (Generalitat de Catalunya) through Project No. 2021-SGR-00450, and J.C. was also supported by an ICREA-Academia award. L.R. and S.S. acknowledge support from ENS de Lyon and CNRS. We are grateful to Nicolas Meunier for making key contributions to the FE solver, originally for a previous project.

APPENDIX A: HYDRODYNAMIC PROBLEM

Our driven fluid is confined to a Hele-Shaw cell of spatially varying height $b(x, y)$, which accounts for the mesa-shaped constriction. The y axis of this cell is also tilted with respect to the ground at an angle $\alpha > 0$, leading to an effective gravitational force: $-g_e \rho \hat{y}$, where $g_e = g \sin \alpha$. The governing equations read

$$\mathbf{u} = \frac{k}{\mu} (-\nabla p - g_e \rho \hat{y}), \quad \text{in } \Omega(t), \quad (\text{A1})$$

$$\nabla \cdot (b \mathbf{u}) = 0, \quad \text{in } \Omega(t), \quad (\text{A2})$$

$$p = \gamma \left(\frac{\pi}{4} \kappa - \frac{2}{b} \right), \quad \text{on } \Gamma_1(t), \quad (\text{A3})$$

$$u_x = 0, \quad \text{on } \Gamma_2(t) \text{ and } \Gamma_4(t), \quad (\text{A4})$$

$$u_y = V_0, \quad \text{on } \Gamma_3(t). \quad (\text{A5})$$

In the zero Re limit, and under the lubrication approximation, the gap-averaged flow \mathbf{u} is determined by Darcy's law with permeability $k = b^2/12$ [Eq. (A1)]. The incompressibility condition, which projects the three-dimensional (3D) divergence on the 2D domain $\Omega(t)$, is given by Eq. (A2). Here p represents the difference between the fluid pressure in $\Omega(t)$ and the air pressure outside $\Omega(t)$, which is assumed constant due to negligible viscosity. To define the boundary conditions, it is convenient to distinguish between four sections of $\Gamma(t)$. In our notation, Γ_1 refers to the top free-boundary (the oil-air interface) that traverses the constriction. Normal force balance on this section is given by the Young-Laplace condition, Eq. (A3), with the $\pi/4$ geometric correction to the in-plane curvature [36]. This condition assumes perfect wetting ($\cos \theta = 1$) and zero thickness of the wetting layer. Next, we denote by Γ_2 and Γ_4 the rigid side walls of the cell, i.e., $x = \pm W/2$. The no-flux condition on these walls is given by Eq. (A4). Lastly, Γ_3 refers to the rear end of the domain under consideration, located at $L = 100$ mm behind the back-end of the mesa. There, we impose that the fluid moves with the driving velocity $V_0 \hat{y}$ [Eq. (A5)].

The boundary-value problem above is accompanied by the kinematic condition, stating that the normal velocity of the free interface V_n is determined by the normal flow

$$V_n = \mathbf{u} \cdot \mathbf{n} \quad \text{on } \Gamma_1(t). \quad (\text{A6})$$

APPENDIX B: FINITE-ELEMENT SIMULATIONS

Our simulations of the full hydrodynamic problem are based on the finite element method (FEM). Explained briefly, the PDE domain is partitioned into a finite number of triangular elements on which a piecewise polynomial solution for \mathbf{u} and p is computed. The calculus used to find this solution relies on the variational (or “weak”) formulation of the corresponding PDE. To capture the evolving shape dynamics, we utilize a stabilized moving-mesh scheme that features our implicit treatment of the curvature term [39,40]. Furthermore, we define a dynamic adaptive mesh that is refined specifically around the sharp mesa edges and the free boundary Γ_1 . The rest of this section is organized as follows. We first write the time-discrete version of the original continuous equations. We then present the variational form of our time-discrete PDEs. Lastly, we explain the spatial discretization into finite elements and discuss some key aspects of our moving-mesh method.

1. Time discretization

We introduce a time step Δt and solve, in each time iteration i , for the implicit fluid flow \mathbf{u}^{i+1} and pressure p^{i+1} based on the current domain configuration Ω^i and its interface Γ^i (with normal \mathbf{n}^i). The time-discrete version of Eqs. (A1) to (A5) is given by

$$\frac{\mu}{k} \mathbf{u}^{i+1} + \nabla p^{i+1} + g_e \rho \hat{\mathbf{y}} = 0, \quad \text{in } \Omega^i, \quad (\text{B1a})$$

$$b \nabla \cdot \mathbf{u}^{i+1} + \nabla b \cdot \mathbf{u}^{i+1} = 0, \quad \text{in } \Omega^i, \quad (\text{B1b})$$

$$p^{i+1} \mathbf{n}^i = \gamma \left(\frac{\pi}{4} \tilde{\mathbf{H}}^{i+1} - \frac{2}{b} \right), \quad \text{on } \Gamma_1^i, \quad (\text{B1c})$$

$$u_x^{i+1} = 0, \quad \text{on } \Gamma_2^i \text{ and } \Gamma_4^i, \quad (\text{B1d})$$

$$u_y^{i+1} = V_0, \quad \text{on } \Gamma_3^i, \quad (\text{B1e})$$

where $\tilde{\mathbf{H}}^{i+1}$ in Eq. (B1c) is a nonlinear function of \mathbf{u}^{i+1} that approximates the curvature vector on the *deformed interface* Γ_1^{i+1} , expressed back on Γ_1^i . This implicit curvature term is designed to overcome a strict time-stepping condition associated with a purely explicit curvature calculation [39,40]. Formally,

$$\tilde{\mathbf{H}}^{i+1} := -\frac{dT^{i+1}}{ds} = -\nabla T^{i+1} \mathbf{t}^i, \quad (\text{B2})$$

where s and \mathbf{t}^i are, respectively, the arc-length coordinate and unit tangent on Γ_1^i , and

$$T^{i+1} := \mathbf{t}^{i+1} \circ (\text{Id} + \Delta t \mathbf{u}^{i+1}) = \frac{(\mathbf{I} + \Delta t \nabla \mathbf{u}^{i+1}) \mathbf{t}^i}{|(\mathbf{I} + \Delta t \nabla \mathbf{u}^{i+1}) \mathbf{t}^i|}$$

is the tangent on Γ_1^{i+1} “pulled back” to Γ_1^i . Note that the nonlinear dependence on \mathbf{u}^{i+1} is handled with a Newton-like method, explained in more detail later.

After computing \mathbf{u}^{i+1} , we propagate the domain with the flow \mathbf{u}^{i+1} , such that

$$\Omega^{i+1} = \varphi^{i+1}(\Omega^i) := (\text{Id} + \Delta t \mathbf{u}^{i+1})(\Omega^i). \quad (\text{B3})$$

This propagation also dictates that any point \mathbf{x}^i on Γ_1^i translates to $\mathbf{x}^{i+1} = \mathbf{x}^i + \Delta t \mathbf{u}^{i+1}(\mathbf{x}^i)$ on Γ_1^{i+1} . The normal component of this operator is essentially a time discrete version of the kinematic condition, Eq. (A6). Note that tangential movement of the interface is irrelevant in the sense of the continuous problem. However, upon spatial discretization, it is quite useful to move boundary vertices with both components of \mathbf{u}^{i+1} .

2. Modified flux condition

To facilitate the weak formulation of the time-discrete problem, we chose an alternative to the flux condition in Eq. (B1e). It is nearly equivalent to impose that the pressure at the inlet or outlet varies constantly in time as follows:

$$p^{i+1} = p_3(t) := \left(\frac{\mu}{k_0} V_0 + g_e \rho \right) (L + y_0 + V_0 t) - \gamma \frac{2}{b_0} \quad \text{on } \Gamma_3, \quad (\text{B4})$$

where Γ_3 corresponds to the line $y = -L$, y_0 is the initial position of Γ_1 and $t = i \Delta t$.

3. Variational (weak) formulation

We present here the weak formulation of the time-discrete problem to be solved via FEM. For brevity, we omit in the following all superscripts (time indices) specified in Eqs. (B1), (B2), and (B4). The Dirichlet conditions in Eq. (B1d) constrain the function space on which we solve

$$\begin{aligned} & \int_{\Omega} \left(\frac{\mu}{k} \mathbf{u} + g_e \rho \hat{y} \right) \cdot \mathbf{v} \, da - \int_{\Omega} p \nabla \cdot \mathbf{v} \, da + \int_{\Gamma_3} p_3(t) \mathbf{v} \cdot \mathbf{n} \, dl - \gamma \int_{\Gamma_1} \frac{2}{b} \mathbf{v} \cdot \mathbf{n} \, dl \\ & + \int_{\Omega} (b \nabla \cdot \mathbf{u} + \nabla b \cdot \mathbf{u}) q \, da + \gamma \frac{\pi}{4} \int_{\Gamma_1} (\nabla \mathbf{v} \mathbf{t}) \cdot T \, dl = 0. \end{aligned} \quad (\text{B5})$$

The goal is to find $p \in L^2(\Omega)$ (the Lebesgue space) and $\mathbf{u} \in H^1(\Omega)^2$ (a two-component Sobolev space H^1) such that Eq. (B5) holds for any arbitrary smooth test functions $\mathbf{v} : \Omega \rightarrow \mathbb{R}^2$ and $q : \Omega \rightarrow \mathbb{R}$.

4. Newton-like method

To handle the nonlinear term T^{i+1} in Eq. (B5) we shall compute the limit of a converging sequence of solutions to a modified linear problem. The linearization of Eq. (B5) is based on a second-order variational expansion of the deformed perimeter [39,40].

In each time step i , we define a sequence $(\mathbf{u}^k)_k$, where $\mathbf{u}^0 = 0$ and $\mathbf{u}^{k+1} \in H^1(\Omega)^2$, $p \in L^2(\Omega)$ are solutions to the following problem:

$$\begin{aligned} & \int_{\Omega} \left(\frac{\mu}{k} \mathbf{u}^{k+1} + g_e \rho \hat{y} \right) \cdot \mathbf{v} \, da - \int_{\Omega} p \nabla \cdot \mathbf{v} \, da + \int_{\Gamma_3} p_3(t) \mathbf{v} \cdot \mathbf{n} \, dl - \gamma \int_{\Gamma_1} \frac{2}{b} \mathbf{v} \cdot \mathbf{n} \, dl \\ & + \int_{\Omega} (b \nabla \cdot \mathbf{u}^{k+1} + \nabla b \cdot \mathbf{u}^{k+1}) q \, da + \gamma \frac{\pi}{4} \int_{\Gamma_1} \left((\nabla \mathbf{v} \mathbf{t}) \cdot T^k + \Delta t \frac{(\nabla \delta \mathbf{u}^{k+1} \mathbf{t}) \cdot (\nabla \mathbf{v} \mathbf{t})}{dS^k} \right) dl = 0, \end{aligned} \quad (\text{B6})$$

for all arbitrary smooth test functions $\mathbf{v} : \Omega \rightarrow \mathbb{R}^2$ and $q : \Omega \rightarrow \mathbb{R}$, and where

$$T^k := \frac{(\mathbf{I} + \Delta t \nabla \mathbf{u}^k) \mathbf{t}}{|(\mathbf{I} + \Delta t \nabla \mathbf{u}^k) \mathbf{t}|}, \quad dS^k := |(\mathbf{I} + \Delta t \nabla \mathbf{u}^k) \mathbf{t}|, \quad \delta \mathbf{u}^{k+1} := \mathbf{u}^{k+1} - \mathbf{u}^k.$$

In our algorithm, Eq. (B6) is solved recursively until the following stopping criterion is satisfied

$$\frac{\int_{\Omega} (\delta \mathbf{u}^{k+1})^2 \, da}{\int_{\Omega} (\mathbf{u}^k)^2 \, da} < \epsilon.$$

We set the tolerance to $\epsilon = 10^{-5}$ and also imposed a minimum of two Newton iterations.

5. Spatial discretization

We cover the domain Ω by a triangulation \mathcal{T}_h (with maximum mesh size h) that is globally conforming, meaning that Γ_h is a piecewise affine approximation of the interface Γ . For computational

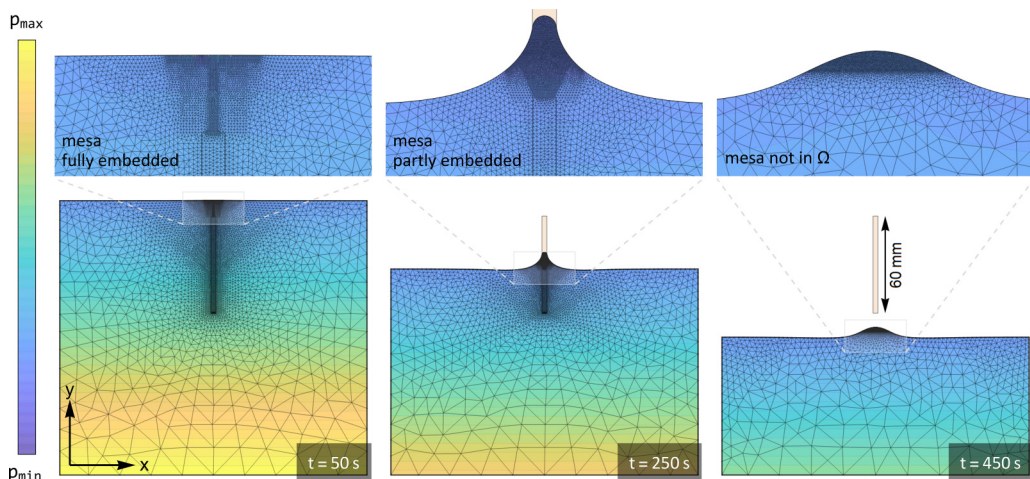


FIG. 6. Mesh and pressure in FE simulation. Snapshots from a typical drainage simulation ($V_0 = -210 \mu\text{m/s}$) showing the adaptive mesh (black) and the resulting pressure field (color-coded contour plot). The mesa constriction is either fully embedded, partly embedded, or out of the oil domain Ω , depending on the progression of the free interface Γ_1 .

efficiency, our mesh is designed to be coarser in the bulk of the domain and much finer along the boundary Γ_1 , particularly, the central segment that is most deformed. We also refine the mesh around the sharp mesa edges that lie inside Ω (see Fig. 6). For robustness, we define b with continuous edges of slope $|\nabla b| = 1$. This means that the side edges, as well as the back-end and front-end of the mesa have a width $\delta b \ll w$. Our adaptive mesh is defined in way that appropriately captures this profile.

In each element $K \in \mathcal{T}_h$, we approximate both components of the velocity $\mathbf{u} \in X := H^1(\Omega)^2$ by a polynomial of degree one enriched with a “bubble” function (a polynomial of degree three defined as the product of the barycentric coordinates in K and vanishing on the faces of K), and the pressure $p \in M := L^2(\Omega)$ by a polynomial of degree one. These approximations are continuous across the element faces except for the pressure at the interface Γ_h . Formally, our functional spaces are

$$\begin{aligned} X_h &= \{\mathbf{v}_h \in C^0(\bar{\Omega})^2; \forall K \in \mathcal{T}_h, \mathbf{v}_{h|K} \in (\mathbb{P}_1 + b_K)^2\} \cap X, \\ M_h &= \{q_h \in C^0(\bar{\Omega}); \forall K \in \mathcal{T}_h, q_{h|K} \in \mathbb{P}_1\} \cap M, \end{aligned}$$

such that $\mathbf{u}, \mathbf{v} \in X_h$ and $p, q \in M_h$ in Eq. (B6).

We run our simulations using the open-source program FREEFEM++ [38]. Given a boundary discretization, this program generates the mesh and also the basis of “hat functions” that span our discrete functional spaces. The integrals in our variational equation are consequently converted to sums, which form a large system of coupled algebraic equations. The associated matrix problem is solved via the SPARSEsolver in FREEFEM++.

6. Moving mesh

After computing \mathbf{u}^{i+1} in \mathcal{T}_h^i , one must propagate the domain via Eq. (B3). The MOVEMESH function translates each vertex k from $\mathbf{x}_k^i \in \mathcal{T}_h^i$ to $\mathbf{x}_k^{i+1} = \mathbf{x}_k^i + \Delta t \mathbf{u}^{i+1}(\mathbf{x}_k^i) \in \mathcal{T}_h^{i+1}$. This step moves and deforms the triangular elements that make up the mesh. Over time, depending on the degree of variance in \mathbf{u} (as determined by the physics) and the choice of Δt , this could lead to a poor spatial discretization, particularly around the mesa edges and Γ_1 . Hence, we chose to remesh our domain at the end of each time step.

7. Remeshing

Our remeshing algorithm immediately follows the propagation step. It is designed to retain a desired distribution of elements throughout the course of the simulation, both in the bulk and on the boundary. It is important to mention at this point that the most sensitive quantity in our problem is the curvature κ on Γ_1 . A standard remeshing of this boundary, based on a linear interpolation of nodes, leads to significant numerical error. To avoid this, we define a custom remeshing of Γ_1^{i+1} that aims to preserve the “integrity” of the shape. In practice, we keep most boundary vertices intact (meaning moved with \mathbf{u}^{i+1} but not remeshed) and only redefine a central segment of Γ_1^{i+1} that is highly deformed by the mesa. The new set of vertices is computed from a cubic spline interpolation of the propagated nodes of this segment. The new bulk triangulation is then subordinate to the updated boundary discretization as well as the fixed outline of the mesa edges that lie inside Ω . Note also that the extent of this refined outline varies in time based on the current position of Γ_1 .

APPENDIX C: LINEAR STABILITY AT CONSTANT GAP

The following analysis is not new, but it is presented here for completeness. Our objective is to explain the stability criterion for our experiments and also derive an explicit formula describing the decay of linear interface modulations with respect to the flat configuration. We consider the classical Hele-Shaw problem, such that the gap height is constant: $b = b_0$. Note that this is the case in our drainage displacements after the interface depins from the back-end of the mesa.

Assume that the sharp interface Γ_1 , in the moving frame, can be described by $h(x, t) = y - V_0 t$ for $t > 0$ and $x \in [-W/2, W/2]$. Here, h accounts for all shape deviations from the flat configuration. Reflecting the symmetry in our problem, we expand h as a cosine series

$$h = \sum_{m=1}^{\infty} h_m(t) \cos(q_m x), \quad q_m := \frac{2\pi m}{W}. \quad (\text{C1})$$

It follows from Darcy’s law, Eq. (A1), and normal force balance, Eq. (A3), that the resulting pressure field in $\Omega(t)$ is a sum of three contributions

$$p = -\left(g_e \rho + \frac{\mu}{k_0} V_0\right) \bar{y} - \frac{2\gamma}{b_0} + \delta p(x, \bar{y}, t), \quad (\text{C2})$$

where \bar{y} is the vertical coordinate in the moving frame. The first term accounts for the hydrostatic pressure and the viscous pressure gradient associated with a uniform flow of the fluid. The second term balances the capillary pressure associated with the constant meniscus curvature. The third term, δp , captures the pressure deviations resulting from the deformation of the planar interface.

At constant gap height, Eqs. (A1) and (A2) lead to $\nabla^2 p = 0$, and thus

$$\nabla^2 \delta p = 0 \quad \text{in } \Omega(t). \quad (\text{C3})$$

The boundary conditions for δp are obtained from substituting Eq. (C2) back in Eqs. (A3) and (A5):

$$\delta p = \frac{\pi}{4} \gamma \kappa + \left(\frac{\mu}{k_0} V_0 + g_e \rho\right) h, \quad \text{on } \bar{y} = h(x, t), \quad (\text{C4})$$

$$\partial_x \delta p = 0, \quad \text{on } x = \pm W/2, \quad (\text{C5})$$

$$\partial_y \delta p = 0, \quad \text{on } \bar{y} = -L - V_0 t. \quad (\text{C6})$$

Note that the last condition reflects the fact that the inlet, which is stationary in the laboratory, is moving in the \bar{y} frame. The generic solution to Eq. (C3), that satisfies Eqs. (C5) and (C6),

is given by

$$\delta p = \sum_{m=1}^{\infty} \delta p_m(t) \cosh[q_m(\bar{y} + L + V_0 t)] \cos(q_m x). \quad (\text{C7})$$

Next, we find $\{\delta p_m\}$ by imposing Eq. (C4). To first order in δp and h , the pressure and curvature on the boundary Γ_1 are given by

$$\delta p \simeq \delta p(\bar{y} = 0) = \sum_{m=1}^{\infty} \delta p_m(t) \cosh[q_m(L + V_0 t)] \cos(q_m x), \quad (\text{C8})$$

$$\kappa \simeq -\partial_{xx} h(x, t) = \sum_{m=1}^{\infty} q_m^2 h_m(t) \cos(q_m x). \quad (\text{C9})$$

Substituting Eqs. (C8) and (C9) back in Eq. (C4) gives

$$\delta p_m(t) = \text{sech}[q_m(L + V_0 t)] \left(\frac{\pi \gamma}{4} q_m^2 + \frac{\mu}{k_0} V_0 + g_e \rho \right) h_m(t). \quad (\text{C10})$$

To first order in h , the normal velocity of the interface \bar{V}_n and the normal component of the flow $\bar{\mathbf{u}}$ (in the moving frame) are

$$\bar{V}_n \simeq \partial_t h(x, t) = \sum_{m=1}^{\infty} h'_m(t) \cos(q_m x), \quad (\text{C11})$$

$$\bar{\mathbf{u}} \cdot \mathbf{n} \simeq -\frac{k_0}{\mu} \partial_{\bar{y}} \delta p(\bar{y} = 0) = -\frac{k_0}{\mu} \sum_{m=1}^{\infty} \tanh[q_m(L + V_0 t)] q_m \left(\frac{\pi \gamma}{4} q_m^2 + \frac{\mu}{k_0} V_0 + g_e \rho \right) h_m(t) \cos(q_m x). \quad (\text{C12})$$

Lastly, substituting Eqs. (C11) and (C12) back in Eq. (A6) yields

$$h'_m(t) = \omega_m h_m(t), \quad (\text{C13})$$

where

$$\omega_m = -\frac{k_0}{\mu} \tanh[q_m(L + V_0 t)] q_m \left(\frac{\pi \gamma}{4} q_m^2 + \frac{\mu}{k_0} V_0 + g_e \rho \right) \simeq -\frac{\gamma}{\mu} q_m \left(\frac{\pi k_0}{4} q_m^2 + \text{Ca} + \text{Bo} \right) \quad (\text{C14})$$

is the dispersion relation. For $L + V_0 t > W$, the \tanh factor tends to 1 and is thus ignored. The growth rates ω_m , which determine the temporal decay of linear deformations, depend linearly on Ca . It follows that, in drainage ($\text{Ca} < 0$), the depinning from the mesa would be slower for increasing speeds.

The linear stability of the flat interface is thus determined by the sign of $\text{Ca} + \text{Bo}$. Note that, in the unstable regime, the marginal mode is

$$q^* = \sqrt{-\frac{\text{Ca} + \text{Bo}}{\pi k_0/4}}.$$

Hence, $\lambda^* = 2\pi/q^*$ is the marginal wavelength: sinusoidal modulations of wavelength greater than λ^* are linearly unstable while those smaller are linearly stable.

In conclusion, if we denote by $\{a_m\}$ the cosine series expansion of $h(x, t_0)$ (corresponding, e.g., to the point of depinning from the mesa), we have, for $t > t_0$,

$$h(x, t) = \sum_{m=1}^{\infty} a_m e^{\omega_m(t-t_0)} \cos(q_m x).$$

We used this result to verify the linear depinning dynamics in our FE simulations (not shown).

APPENDIX D: STEADY INTERFACE DEFORMATIONS

We derive here the steadily moving solution, defined such that $\mathbf{u} = V_0 \hat{y}$ in $\Omega(t)$, considering an infinitely long mesa

$$b(x) = b_0 - \delta b \operatorname{rect}(x/w).$$

It follows from Eq. (A1) that the pressure takes the simple form

$$p = -\left(\frac{\mu}{k} V_0 + \rho g_e\right)(y - V_0 t) + C, \quad (\text{D1})$$

where C is a constant that needs to be determined. Note that we disregard the lateral gradient of this pressure profile on the side edges of the mesa, where $\partial_x k^{-1} \propto b^{-3} \partial_x b \neq 0$.

Let $h(x) := y - V_0 t$ describe the steadily moving boundary line Γ_1 . Substituting Eq. (D1) back in Eq. (A3), we obtain

$$-\left(\frac{\mu}{k} V_0 + g_e \rho\right) h(x) + C = \gamma \left(\frac{\pi}{4} \kappa(x) - \frac{2}{b(x)} \right), \quad (\text{D2})$$

where $\kappa(x) = \frac{-h''(x)}{(1+h''(x)^2)^{3/2}}$.

We shall now impose, without loss of generality, that $h = 0$ marks the altitude (in the comoving frame) at which the side ‘‘wings’’ of the interface level out. In the flat limit, far away from the mesa, $h'' \rightarrow 0$, and thus Eq. (D2) is balanced by setting $C = -\gamma 2/b_0$. We now have

$$-\left(\frac{\mu}{k} V_0 + g_e \rho\right) h(x) = \gamma \left(\frac{\pi}{4} \kappa(x) - \frac{2}{b(x)} + \frac{2}{b_0} \right). \quad (\text{D3})$$

This ODE poses a nonlinear ‘‘elastica’’-like problem for the steadily moving boundary line. We first linearize this equation to derive an approximate formula for $h(x)$. Afterwards, we solve the exact nonlinear problem computationally through a dedicated ‘‘shooting method.’’

1. Linearization

To first order in h , h' , h'' , and δb , Eq. (D3) reduces to

$$\left(1 - \ell_c^2 \frac{d^2}{dx^2}\right) h = \frac{8}{\pi} \left(\frac{\ell_c}{b_0}\right)^2 \delta b \operatorname{rect}(x/w), \quad (\text{D4})$$

where

$$\ell_c = \sqrt{\frac{\gamma \pi / 4}{\mu V_0 / k_0 + \rho g_e}} = \sqrt{\frac{k_0 \pi / 4}{\text{Ca} + \text{Bo}}}$$

is the capillary length, which measures the extent of lateral correlations of front modulations [31,33,42]. Note that ℓ_c is real-valued only under stable Saffman-Taylor conditions, meaning $\text{Ca} + \text{Bo} > 0$, and pure imaginary otherwise. In the unstable regime, $2\pi \operatorname{Im}[\ell_c]$ corresponds to the wavelength λ^* of the marginally stable Fourier mode (see Appendix C).

Solving Eq. (D4) in Fourier space, one obtains

$$\hat{h}(q) = \frac{8}{\pi} \left(\frac{\ell_c}{b_0}\right)^2 \delta b \frac{w \operatorname{sinc}(wq/2)}{1 + \ell_c^2 q^2}. \quad (\text{D5})$$

The inverse transform of \hat{h} is found analytically [copy of Eq. (4)]

$$h(x) = \frac{8}{\pi} \left(\frac{\ell_c}{b_0}\right)^2 \delta b \begin{cases} 1 - e^{-w/2\ell_c} \cosh\left(\frac{x}{\ell_c}\right), & |x| \leq \frac{w}{2}, \\ \sinh\left(\frac{w}{2\ell_c}\right) e^{-|x|/\ell_c}, & |x| > \frac{w}{2}. \end{cases} \quad (\text{D6})$$

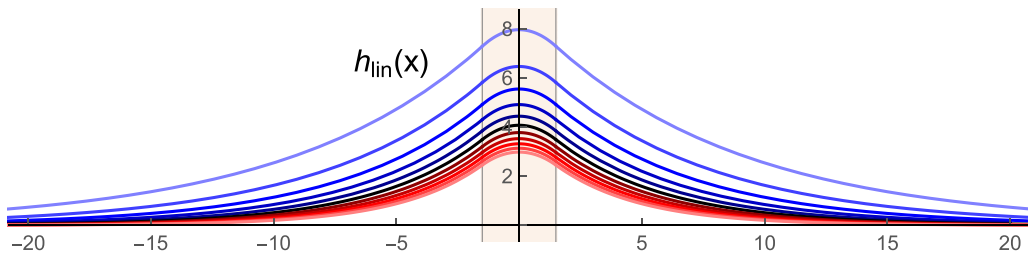


FIG. 7. Linear steady state. We plot the linear profile $h(x)$, defined in Eq. (4), for different values of V_0 . Drainage speeds were set to $V_0 = \{-200, -160, -120, -80, -40\}$ $\mu\text{m/s}$ (light to dark blue) and imbibition speeds were set to $V_0 = \{40, 80, 120, 160, 200\}$ $\mu\text{m/s}$ (dark to light red). The $V_0 = 0$ state is plotted in black. Axes ticks are in mm.

An equivalent expression was derived in Ref. [32] for the case $V_0 = 0$. Figure 7 shows examples of the linear profile for different values of V_0 (drainage in blue, imbibition in red).

We obtain from Eq. (D6) the linear deformation amplitude,

$$\eta_{\text{lin}}(d) = h(0) - h(d) = \frac{8}{\pi} \left(\frac{\ell_c}{b_0} \right)^2 \left[1 - e^{-w/2\ell_c} - \sinh \left(\frac{w}{2\ell_c} \right) e^{-d/\ell_c} \right] \delta b. \quad (\text{D7})$$

We plot $\eta_{\text{lin}}(9 \text{ mm})$ as a function of V_0 in Fig. 4 (dashed line). We recover also the expression derived in [31] for $d \rightarrow \infty$,

$$\eta_{\text{lin}}(\infty) = h(0) = \frac{8}{\pi} \left(\frac{\ell_c}{b_0} \right)^2 (1 - e^{-w/2\ell_c}) \delta b. \quad (\text{D8})$$

In our regime of interest, we find that the solution given by Eq. (D6) is, in fact, inconsistent with the assumption $|h'| \ll 1$, which underlies Eq. (D4). The slope of $h(x)$ is maximized on the side edges of the mesa. Per Eq. (D6), one has

$$|h'|_{\text{max}} = |h'(x = \pm w/2)| = \frac{8}{\pi} \frac{\ell_c \delta b}{b_0^2} \sinh \left(\frac{w}{2\ell_c} \right) e^{-w/2\ell_c}.$$

As shown in Fig. 8, we find that $|h'|_{\text{max}}$ of the linear profile is close to 1 and may even exceed 1 under our experimental conditions. The nonlinear solution to Eq. (D3) (discussed in the following subsection) shows that this quantity tends to diverge well before the S-T critical point.

2. Shooting method

The objective here is to obtain more theoretically accurate solutions that go beyond the linear approximation. The idea is to find (i) better agreement with experiments and (ii) a means of validating our dynamic FE simulations at the nonlinear level. To this end, we developed a method for finding the most physically relevant solution to Eq. (D3). To solve this ODE computationally, one must specify two boundary conditions. We chose the following for convenience:

$$h'(0) = 0, \quad h(0) = h_0. \quad (\text{D9})$$

The first condition reflects the fact that the profile of interest is symmetric about the y axis with a maximum at $x = 0$ (the tip of the protrusion). However, the amplitude at this point is not known *a priori*. We thus employ a “shooting method” that consists of the following. (1) Generate a sequence of numerical ODE solutions corresponding to different values of h_0 . (2) Find the value of h_0 that produces the optimal solution, meaning the one for which $h \rightarrow 0$ as $x \rightarrow \pm\infty$. In practice, we vary h_0 as to minimize $|h(\pm W/2)|$. Our goal is to trace out a branch of optimal solutions corresponding to different values of V_0 (the control parameter in this study). To do this efficiently, we further employ

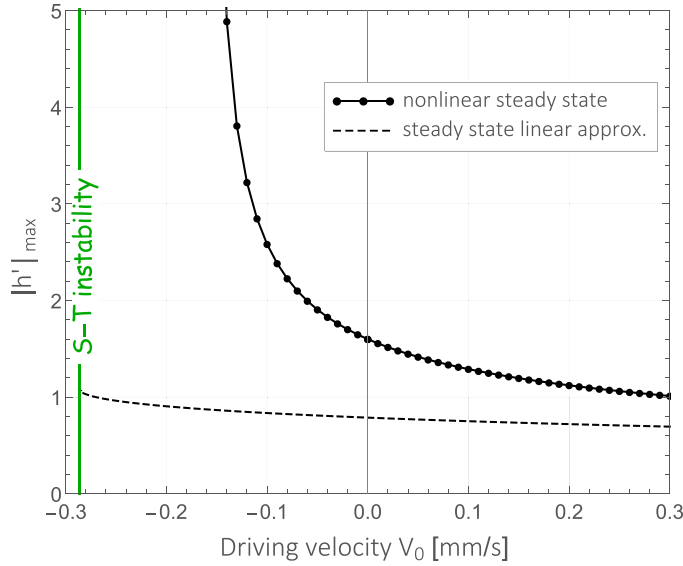


FIG. 8. Invalidity of the linear curvature assumption. The maximal slope of the linear and nonlinear steady state is plotted as a function of the driving speed. Other parameters are fixed at their experimental values. Green line marks the threshold of the Saffman-Taylor instability, where $Ca = -Bo$.

a parametric continuation procedure. We iterate small steps in V_0 and use previously computed values of h_0 to generate a good initial guess for the amplitude in the next iteration of the velocity. We developed a tool in MATHEMATICA, based on the NDSOLVE and INTERPOLATE functions, that facilitates this process.

As we have done in our FE simulations, we modify the gap profile to obtain robust computational solutions. Specifically, we avoid the discontinuity in b along the side edges of the mesa by defining

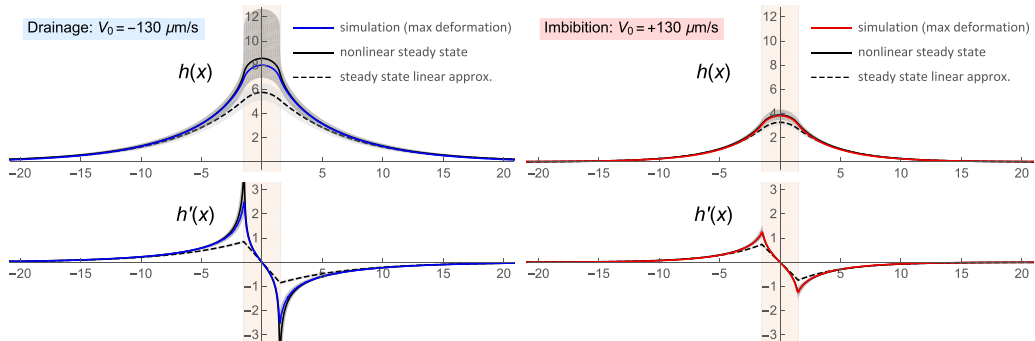


FIG. 9. Steady state profiles. Top panels: The nonlinear steady-state solution (black, obtained via our “shooting method”) and its explicit linear approximation [dashed, Eq. (4)] are compared with the maximal interface deformation in drainage or imbibition simulations (blue or red). Confidence levels on the first represent the deviation due to cumulative uncertainty in our measured parameters (not including error in V_0). Axes ticks are in mm. Bottom panels: Comparison of the profile derivatives.

continuous edges with slope $|b'(x)| = 1$, i.e.,

$$b(x) = b_0 - \begin{cases} \delta b, & |x| \leq \frac{w}{2} - \delta b, \\ \frac{w}{2} - |x|, & \frac{w}{2} - \delta b < |x| \leq \frac{w}{2}, \\ 0, & |x| > \frac{w}{2}. \end{cases} \quad (\text{D10})$$

Note that this choice does not significantly modify the geometry since $\delta b \ll w$.

In Fig. 9 we compare the linear and nonlinear steady state prediction with the maximal interface deformation captured in our FE simulations. This figure exemplifies the strengths and weaknesses of the explicit linear approximation, Eq. (D6). More specifically, for the relevant drainage speeds in this study, the linear approximation fails to capture the observed vertical elongation of the interface along the side edges of the mesa. As noted also in the main text, we expect the FE interface to agree with the nonlinear ODE solution (black) only in cases where the dynamical system had actually reached steady state. For the examples shown in Fig. 9, this happens in imbibition (red) but not in drainage (blue).

-
- [1] M. Sahimi, *Flow and Transport in Porous Media and Fractured Rock* (Wiley, New York, 2011).
 - [2] J. Feder, E. G. Flekkoy, and A. Hansen, *Physics of Flow in Porous Media* (Cambridge University Press, Cambridge, England, 2022).
 - [3] M. J. Blunt, *Multiphase Flow in Permeable Media. a Pore-Scale Perspective* (Cambridge University Press, Cambridge, England, 2017).
 - [4] K. Singh, M. Jung, M. Brinkmann, and R. Seemann, Capillary-dominated fluid displacement in porous media, *Annu. Rev. Fluid Mech.* **51**, 429 (2019).
 - [5] R. Ababou, *Capillary Flows in Heterogeneous and Random Porous Media* (Wiley, New York, 2022).
 - [6] B. Levaché and D. Bartolo, Revisiting the saffman-taylor experiment: Imbibition patterns and liquid-entrainment transitions, *Phys. Rev. Lett.* **113**, 044501 (2014).
 - [7] R. Holtzman and E. Segre, Wettability stabilizes fluid invasion into porous media via nonlocal, cooperative pore filling, *Phys. Rev. Lett.* **115**, 164501 (2015).
 - [8] M. Trojer, M. L. Szulczewski, and R. Juanes, Stabilizing fluid-fluid displacements in porous media through wettability alteration, *Phys. Rev. Appl.* **3**, 054008 (2015).
 - [9] B. Zhao, C. W. MacMinn, and R. Juanes, Wettability control on multiphase flow in patterned microfluidics, *Proc. Natl. Acad. Sci. USA* **113**, 10251 (2016).
 - [10] B. K. Primkulov, S. Talman, K. Khaleghi, A. R. Shokri, R. Chalaturnyk, B. Zhao, C. W. Macminn, and R. Juanes, Quasistatic fluid-fluid displacement in porous media: Invasion-percolation through a wetting transition, *Phys. Rev. Fluids* **3**, 104001 (2018).
 - [11] R. Lenormand, E. Touboul, and C. Zarcone, Numerical models and experiments on immiscible displacements in porous media, *J. Fluid Mech.* **189**, 165 (1988).
 - [12] R. Lenormand, Liquids in porous media, *J. Phys.: Condens. Matter* **2**, SA79 (1990).
 - [13] R. Hughes and M. Blunt, Pore scale modeling of rate effects in imbibition, *Transp. Porous Media* **40**, 295 (2000).
 - [14] C. Odier, B. Levaché, E. Santanach-Carreras, and D. Bartolo, Forced imbibition in porous media: a fourfold scenario, *Phys. Rev. Lett.* **119**, 208005 (2017).
 - [15] R. Hu, D. S. Wu, Z. Yang, and Y. F. Chen, Energy conversion reveals regime transition of imbibition in a rough fracture, *Geophys. Res. Lett.* **45**, 8993 (2018).
 - [16] P. G. de Gennes, Imperfect Hele - Shaw cells, *J. Phys. France* **47**, 1541 (1986).
 - [17] A. B. Thompson, A. Juel, and A. L. Hazel, Multiple finger propagation modes in Hele-Shaw channels of variable depth, *J. Fluid Mech.* **746**, 123 (2014).
 - [18] R. Brandão and J. A. Miranda, Capillary and geometrically driven fingering instability in nonflat Hele-Shaw cells, *Phys. Rev. E* **95**, 033104 (2017).

- [19] H. S. Rabbani, D. Or, Y. Liu, C. Y. Lai, N. B. Lu, S. S. Datta, H. A. Stone, and N. Shokri, Suppressing viscous fingering in structured porous media, *Proc. Natl. Acad. Sci. USA* **115**, 4833 (2018).
- [20] A. Paterson, M. Fermigier, P. Jenffer, and L. Limat, Wetting on heterogeneous surfaces: Experiments in an imperfect Hele-Shaw cell, *Phys. Rev. E* **51**, 1291 (1995).
- [21] A. Paterson and M. Fermigier, Wetting of heterogeneous surfaces: Influence of defect interactions, *Phys. Fluids* **9**, 2210 (1997).
- [22] A. Gaillard, J. S. Keeler, G. Le Lay, G. Lemoult, A. B. Thompson, A. L. Hazel, and A. Juel, The life and fate of a bubble in a geometrically perturbed Hele-Shaw channel, *J. Fluid Mech.* **914**, A34 (2021).
- [23] N. Shmakova, T. Chevalier, A. Puisto, M. Alava, C. Raufaste, and S. Santucci, Quasi-two-dimensional foam flow through and around a permeable obstacle, *Phys. Rev. Fluids* **5**, 093301 (2020).
- [24] H. Schütt and H. Spetzler, Capillary crack imbibition: A theoretical and experimental study using a Hele-Shaw cell, *Pure Appl. Geophys.* **158**, 627 (2001).
- [25] X. Clotet, R. Planet, and J. Ortín, Capillary rise in Hele-Shaw models of disordered media, *J. Colloid Interface Sci.* **377**, 387 (2012).
- [26] J. Soriano, J. J. Ramasco, M. A. Rodríguez, A. Hernández-Machado, and J. Ortín, Anomalous roughening of Hele-Shaw flows with quenched disorder, *Phys. Rev. Lett.* **89**, 026102 (2002).
- [27] J. Soriano, A. Mercier, R. Planet, A. Hernández-Machado, M. A. Rodríguez, and J. Ortín, Anomalous roughening of viscous fluid fronts in spontaneous imbibition, *Phys. Rev. Lett.* **95**, 104501 (2005).
- [28] X. Clotet, J. Ortín, and S. Santucci, Experimental study of stable imbibition displacements in a model open fracture. I. Local avalanche dynamics, *Phys. Rev. E* **93**, 012149 (2016).
- [29] R. Planet, J. M. López, S. Santucci, and J. Ortín, Spatiotemporal organization of correlated local activity within global avalanches in slowly driven interfaces, *Phys. Rev. Lett.* **121**, 034101 (2018).
- [30] X. Clotet, S. Santucci, and J. Ortín, Experimental study of stable imbibition displacements in a model open fracture. II. Scale-dependent avalanche dynamics, *Phys. Rev. E* **93**, 012150 (2016).
- [31] R. Planet, L. Díaz-Piola, and J. Ortín, Capillary jumps of fluid-fluid fronts across an elementary constriction in a model open fracture, *Phys. Rev. Fluids* **5**, 044002 (2020).
- [32] R. Holtzman, M. Dentz, R. Planet, and J. Ortín, The origin of hysteresis and memory of two-phase flow in disordered media, *Commun. Phys.* **3**, 222 (2020).
- [33] E. Pauné and J. Casademunt, Kinetic roughening in two-phase fluid flows through a random Hele-Shaw cell, *Phys. Rev. Lett.* **90**, 144504 (2003).
- [34] E. Álvarez-Lacalle, J. Ortín, and J. Casademunt, Relevance of dynamic wetting in viscous fingering patterns, *Phys. Rev. E* **74**, 025302(R) (2006).
- [35] F. P. Bretherton, The motion of long bubbles in tubes, *J. Fluid Mech.* **10**, 166 (1961).
- [36] C. W. Park and G. M. Homsy, Two-phase displacement in Hele Shaw cells: Theory, *J. Fluid Mech.* **139**, 291 (1984).
- [37] D. Reinelt and P. Saffman, The penetration of a finger into a viscous fluid in a channel and tube, *SIAM J. Sci. Stat. Comput.* **6**, 542 (1985).
- [38] F. Hecht, New development in freefem++, *J. Numer. Math.* **20**, 251 (2012).
- [39] I. Lavi, Physical modeling of cell motility and morphodynamics, Ph.D. thesis, Sorbonne université, 2019.
- [40] I. Lavi, N. Meunier, and O. Pantz, Implicit like time discretization for the one-phase hele-shaw problem with surface tension, [arXiv:2305.06180](https://arxiv.org/abs/2305.06180).
- [41] J. F. Joanny and P.-G. de Gennes, A model for contact angle hysteresis, *J. Chem. Phys.* **81**, 552 (1984).
- [42] M. Dubé, M. Rost, K. R. Elder, M. Alava, S. Majaniemi, and T. Ala-Nissila, Liquid conservation and non-local interface dynamics in imbibition, *Phys. Rev. Lett.* **83**, 1628 (1999).